Shape memory behavior in Fe$_3$Al-modeling and experiments

A. Ojha[a], S. Alkan[a], L. Patriarca[a], H. Sehitoglu[a]* and Y. Chumlyakov[b]

[a]Department of Mechanical Science and Engineering, University of Illinois at Urbana-Champaign, 1206 W. Green Street, Urbana, IL 61801, USA; [b]Siberian Physical Technical Institute, Revolution Sq. 1, Tomsk, 634050, Russia

1. Introduction

Considerable emphasis has been devoted to materials undergoing reversible phase transformations [1]. Less emphasis has been devoted to materials that show reversibility associated with slip deformation. The reversible deformation can lead to pseudoelastic (or superelastic) behaviour if forward and reverse slip can occur with small hysteresis. Pseudoelasticity refers to the recovery of the residual plastic strains upon unloading, and is attributed to the thermoelastic martensitic transformation in most of the shape memory alloys (SMAs). However, the Fe$_3$Al and Fe$_3$Ga with D0$_3$ structure are found to exhibit pseudoelasticity in the absence of martensitic transformation, and strains of few per cent can be recovered [2–4]. The advantage of these alloys compared to the SMAs is the potentially large pseudoelastic temperature range. Reversible slip is due to the to and fro motion of the $a/4\langle 1\,1\,1 \rangle$ superpartials associated with the antiphase boundary (APB) energy [5–7], and is commonly referred to as 'APB pseudoelasticity'. The APB energy arises on a plane where atoms are arranged in an opposite order compared to the perfect lattice. During loading, the independently moving $a/4\langle 1\,1\,1 \rangle$ superpartial leaves behind itself an APB, which then pulls back the superpartial upon unloading.

*Corresponding author. Email: huseyin@illinois.edu

Since strain recovery is a result of the reversible motion of dislocations, it can occur under a wide temperature range. On the contrary, the pseudoelasticity in SMAs, for example, NiTi, occurs by the martensitic transformation and is limited to the tempera-ture above the austenite finish temperature (A_f) over a narrow temperature range.

Pseudoelasticity in $D0_3$ crystals has been of recent interest [2,3,7–12]. All works have been experimental; however, theoretical derivations and atomistic/continuum treat-ments to explain the stress magnitudes have been missing. In the current paper, we compare the modelling efforts with the experimental observations and investigate the parameters governing pseudoelasticity in Fe_3Al. Utilizing novel digital image correla-tion (DIC) techniques, single crystal orientations and composition, we precisely pinpoint the stress required to initiate slip in Fe_3Al unlike the general methodology where slip stress is assumed to be at 0.2% strain offset of the macroscopic stress–strain curve. Concurrently, we calculate the energy barriers (generalized stacking fault energy, GSFE) associated with the $\{1\ 1\ 0\}\langle1 1\ \ 1\rangle$ and $\{1\ 1\ 2\}\langle1 1\ \ 1\rangle$ slips from density functional theory (DFT) calculations at an atomic scale and incorporate it into the modified Peierls–Nabarro (PN) formalism based on anisotropic calculations to predict the slip stress and the recovery stress. We consider the forward and the reverse slip nucleation stresses on $\{1\ 1\ 2\}\langle1 1 1\rangle$ system both for twinning and antitwinning senses noting the asymmetry of the energy barriers in these two cases. We note that the correct assessment of lattice parameter and elastic constants is required to obtain the stress quantities accurately. We, therefore, undertake these calculations using first principles, and for the first time, incorporate the high anisotropy of Fe_3Al in the stress calculations. The theoretically obtained slip stress magnitudes are then compared to the experimental values showing excellent agreement.

Figure 1(a) and (b) show the atomic arrangement in $D0_3$ Fe_3Al. The $D0_3$ structure consists of eight cubic sublattices. Four sublattices are B2-like structures, while the remaining are of pure bcc types. Each subcell consists of Fe atoms in the corners. Four of the subcells consist of Fe atoms in the centre, while the remaining four subcells have Al atoms in the centre. Figure 1(a) and (b) also show the possible slip systems, $\{1\ 1\ 0\}\langle1 1 1\rangle$ and $\{1\ 1\ 2\}\langle1 1 1\rangle$, where $a/4\langle1 1 1\rangle$ dissociated partials form an APB energy. Three distinct $a\langle1 1 1\rangle$ dislocation configurations (modes) have been observed using *in situ* TEM experiments, as schematically shown in Figure 1(c)–(e) [8,13]. Figure 1(c) shows the mode I dislocation configuration where an uncoupled superpartial leaves behind the nearest-neighbour antiphase boundary (NNAPB) upon loading. In mode II (Figure 1(d)), coupled $a/4\langle1 1 1\rangle$ superpartial dislocations move in pair dragging behind the next-nearest-neighbour antiphase boundary (NNNAPB) energy, while in mode III (Figure 1(e)), four superpartials move in group leaving behind NNAPB and NNNAPB.

The choice of dislocation configuration operating in Fe_3Al depends on the composi-tion of the alloy and the deformation temperature [4]. Mode I dislocation configuration results in a high recovery ratio (r) exhibiting perfect pseudoelasticity when Al concen-tration is around 23 at.% [14]. The recovery ratio is a measure of pseudoelasticity of a material, and is defined as the ratio of difference of the maximum plastic strain and the residual strain to that of the maximum plastic strain. When Al concentration increases from 23 at.%, mode II and mode III dislocation configurations start to appear, thus reducing the recovery ratio. This is because NNNAPB energy bounding the coupled partials in mode II is low such that the partials are difficult to be pulled back during
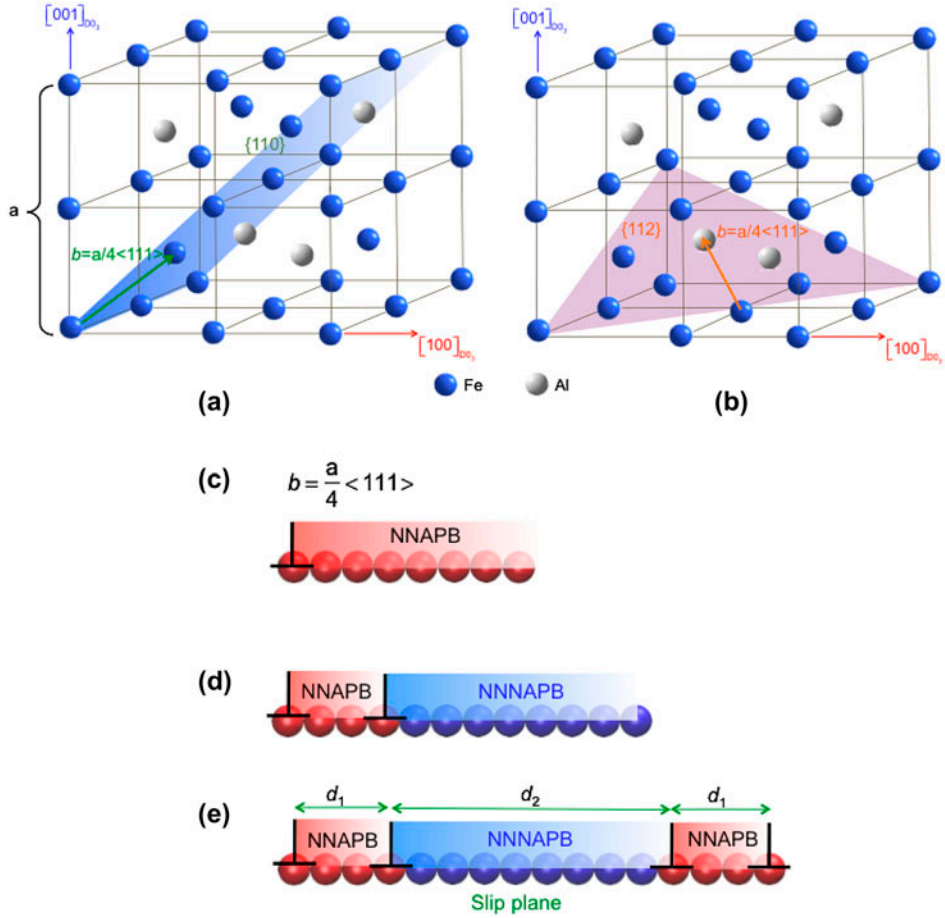
Figure 1. (colour online) D0$_3$ lattice structure of Fe$_3$Al showing (a) $\{1\,1\,0\}\langle1\,1\,1\rangle$ slip system (b) $\{1\,1\,2\}\langle1\,1\,1\rangle$ slip system. The length of the arrow gives the magnitude of the partial dislocation with Burgers vector $b = a/4\langle1\,1\,1\rangle$ (c) Mode I dislocation configuration, where uncoupled $a/4$ $\langle1\,1\,1\rangle$ superpartials leave behind NNAPB ('a' is the lattice constant) (d) Mode II dislocation configuration where paired superpartials leave behind NNNAPB (e) Mode III dislocation configuration where $a\langle1\,1\,1\rangle$ superdislocation dissociates into four $a/4\langle1\,1\,1\rangle$ dislocations.

unloading [4]. Similarly, in mode III, there is no APB left behind the superpartials, and the recovery ratio is well below 20%. The recovery ratio depends on the deformation temperature as well. For example, in Fe-24.4at.%Al, the recovery ratio is observed to be well above 80% in the temperature range 173–473 K and decreases rapidly to below 20% in other temperature intervals [15].

In this work, the crystal orientation of the Fe$_3$Al single crystals was selected in order to activate one primary slip system. We conducted uniaxial tensile and compressive experiments using high resolution DIC strain measurements in order to pinpoint the critical stress required to initiate slip, τ_p and the recovery start stress, τ_r. As the slip is initially active at microscale, DIC strain measurements allow to precisely identify the

local stress–strain behaviour of the alloy providing an accurate measure of the stress required to nucleate slip. In the research community, DIC has been extensively used to measure *real-time* (*in situ*) strain fields for different applications such as slip/twin nucleation, fatigue damage initiation and crack closure measurements [16–19]. For these applications, the typical image resolution is approximately 1–2 μm/px. For other applications where higher image resolutions are required (for example, for studying twin/slip and grain boundary/slip interactions), the images are captured *ex situ* (out of the load frame) under the optical microscope. In these experiments, the images have higher resolutions (up to 0.2 μm/px) with the drawback to measure only the residual strains. Since in Fe_3Al, slip occurs at very small scales, it is necessary to adopt high image resolutions in order to precisely capture the slip activation and recovery. In the present work, we use a special SEMtester load frame for tensile experiments mounted under an optical microscope in order to measure real time strain field measurements at high resolution. These strain measurements are extremely important for materials exhibiting pseudoelasticity since no residual deformation can be detected in the unloaded condition even at high image resolution. Real-time strain fields are used to establish the critical stresses and to verify the activation of one primary slip system.

In the following sections, we discuss our atomistic/DFT approach to calculate the NNAPB and NNNAPB energy values associated with the moving superpartial dislocations. We present the detailed mesoscale elastic calculations to establish the slip start stress and the recovery start stress in Fe_3Al. We then compare our theoretically obtained stress values with the experimental observations in Fe_3Al single crystals.

2. The current approach

2.1. *Atomistic simulations*

The first principles DFT calculations were carried out to calculate the systems total energy. We utilized the Vienna ab initio Simulations Package with the projector augmented wave method and the generalized gradient approximation as implementations of DFT [20,21]. In our calculations, we used $9 \times 9 \times 9$ Monkhorst Pack *k*-point meshes for the Brillouin-zone integration to ensure the convergence of results. Ionic relaxation was performed by a conjugate gradient algorithm. The energy cut-off of 360 eV was used for the plane-wave basis set. The total energy was converged to less than 10^{-5} eV per atom. For GSFE calculations, a full internal atoms relaxation including perpendicular and parallel directions to the fault plane was allowed for minimizing the short-range interaction between the misfitted layers in the vicinity of the fault plane. During the relaxation process, the total energy of the deformed crystal was minimized.

2.2. *Lattice constant of $D0_3$ Fe_3Al*

We obtained the energy variation of the $D0_3$ crystal with respect to different lattice parameters in our simulations, as shown in Figure 2. The equilibrium lattice constant corresponding to the minimum structural energy was obtained as 5.782 Å. Table 1 shows the lattice constant obtained through DFT calculations which are within 2% of the experimentally observed values. The Burgers vector of the dissociated superpartial based on the DFT lattice constant is also presented in Table 1.
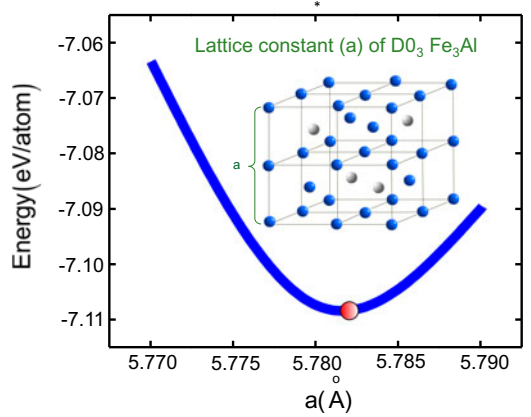
Figure 2. (colour online) Energy variation with lattice constant (a) for $D0_3$ Fe_3Al obtained from DFT calculations.

Table 1. Present DFT calculations and other experimental/DFT lattice parameters and Burgers vector in $D0_3$ Fe_3Al. The DFT value is marked with (*).

	Lattice parameter (Å)			
Structure	This study	Experiments/DFT*	Slip system	Burgers vector (Å)
$D0_3$	5.782	5.79 [22], 5.76 [23]*	$\{1\,1\,0\}\langle 1\,1\,1\rangle$, $\{1\,1\,2\}\langle 1\,1\,1\rangle$	2.49

2.3. Elastic constants calculations of $D0_3$ Fe_3Al

In order to establish the elastic constants, we obtained the total energy variation of the crystal as a function of the volume subjected to three different distortions (strain). The deformation tensors given in Voigt notation and the corresponding energy densities are given in Table 2. The strain parameter δ in Table 2 for each deformation was varied from -0.03 to 0.03 in the present analysis to minimize the errors from higher order terms. After obtaining the total energies E and E_o for the strained and the unstrained lattice, respectively, the parameter $(E - E_o)/V_o$ values were plotted as a function of strain (ε), where V_o is the equilibrium volume. The elastic constants were then extracted from the second-order coefficient fit of the following equation:

$$E(V,\varepsilon) = E(V_o,0) + V_o \sum_{i=1}^{6} \sigma_i \varepsilon_i + \frac{V_o}{2} \sum_{i,j=1}^{6} C_{ij}\varepsilon_i\varepsilon_j + O(\delta^3)$$

Table 2. Distortion matrices and energy densities for elastic constant calculations of $D0_3$ Fe_3Al.

Structure	Distortion matrix	$\Delta E/V_o$
$D0_3$	$\varepsilon_{11} = \varepsilon_{22} = \delta, \varepsilon_{33} = -2\delta$	$3(C_{11} - C_{12})\delta^2 + O(\delta^4)$
	$\varepsilon_{11} = \varepsilon_{22} = \varepsilon_{33} = \delta$	$3/2(C_{11} + 2C_{12})\delta^2 + O(\delta^4)$
	$\varepsilon_{12} = \varepsilon_{21} = \delta/2$	$(C_{44}/2)\delta^2 + O(\delta^4)$

where C_{ij}, σ_i, ε_i are the elastic constants, stress and strain respectively in Voigt notation. The results are graphically shown in Figure 3 and the modulus tensor is provided in Table 3. We note that the DFT results for elastic constants are within 10% of the experimental values.

2.4. *Slip in D0$_3$ F$_3$Al (GSFE)*

The energy associated with the slip is characterized by the GSFE [25,26]. The GSFE for D0$_3$ Fe$_3$Al is obtained by continuously shearing the {1 1 0} or {1 1 2} plane by a displacement of $a/4\langle 1\,1\ \ 1\rangle$, where 'a' is the lattice constant. Figure 4 shows the {1 1 0} stacking sequence and Figure 5 shows the GSFE obtained in the present analysis for {1 1 0}$\langle 1\,1\,1\rangle$ and {1 1 2}$\langle 1\,1\,1\rangle$ slip systems. Three energy terms are noted in Figure 5 – (i) the peak energy corresponding to u/b = 0.5 is γ_{us} defined as the unstable stacking fault energy and represents the energy barrier required to nucleate the first superpartial

dislocation, (ii) γ_{NNAPB} corresponding to u/b = 1 represents the stable energy which is left behind the dislocation, and (iii) γ_{NNNAPB} corresponding to u/b = 2 represents the stable energy value associated with the coupled superpartials. The values of γ_{NNAPB} and γ_{NNNAPB} are of prime interest as they generate stress to pull the dislocations back result-ing in pseudoelasticity. It is worth emphasizing that {$\bar{1}$ 1 2}$\langle 1\,1\,1\rangle$ slip asymmetry is a common characteristic of bcc metals [27–31]. In Figure 5, we obtained the GSFE (γ-curve) for {1 1 2}$\langle 1\,1\,1\rangle$ slip system. We note that γ_{us} for antitwinning sense is higher than that in the twinning sense by 61 mJ m^{-2}. If an applied shear stress causes the slip dislocations to move in the direction required to form a twin, we refer to this shear stress as the 'twinning sense' shear. The 'antitwinning sense' shear is the one that moves the dislocations opposite to the twinning shear. We point to the difference in the
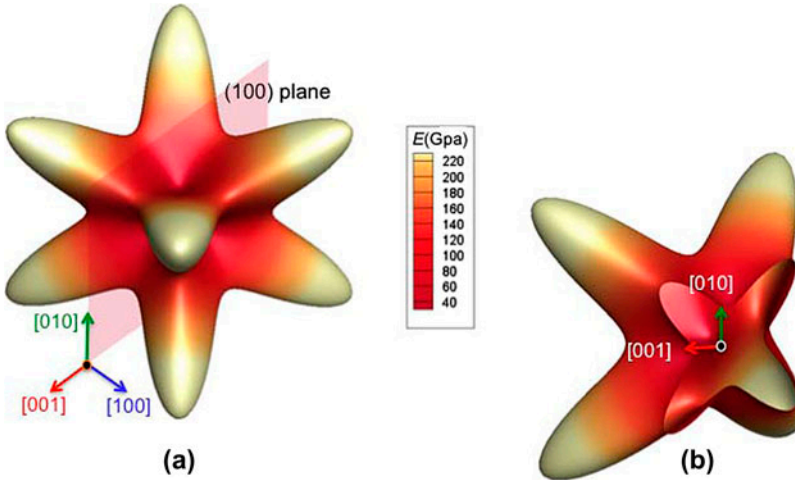

Figure 3. (colour online) Three dimensional representation of elastic moduli (*E*) of D0$_3$ Fe$_3$Al. (a) The (1 0 0) plane is marked with a shaded rectangular surface, (b) cut through the (1 0 0) sur-face through the centre of (a) as viewed along the [$\bar{1}$ 1 1] direction. Note that [0 1 0] and [0 0 1] directions are equivalent for D0$_3$ crystal structure.

Table 3. Elastic constants for $D0_3$ Fe_3Al established using first principles calculations and compared with the experimental values. Note high anisotropy ratio (A) of 7.1.

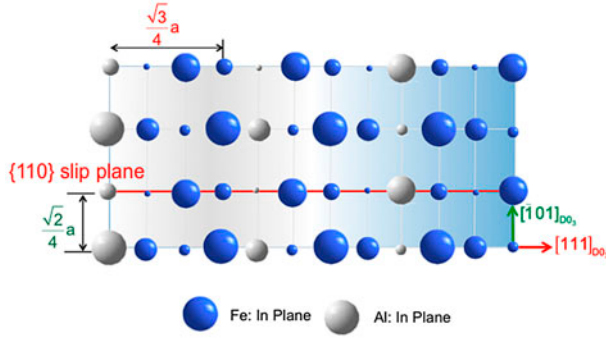| $D0_3$ Fe_3Al	C_{11} (GPa)	C_{12} (GPa)	C_{44} (GPa)	Anisotropy (A)
DFT (this study)	165	125	142	7.1
Experiment [24]	171	131	132	6.6

Figure 4. (colour online) Atomic arrangement of $\{1\,1\,0\}$ plane of $D0_3$ Fe_3Al. The largest spheres represent atoms on plane, while smaller ones represent atoms out of the plane.
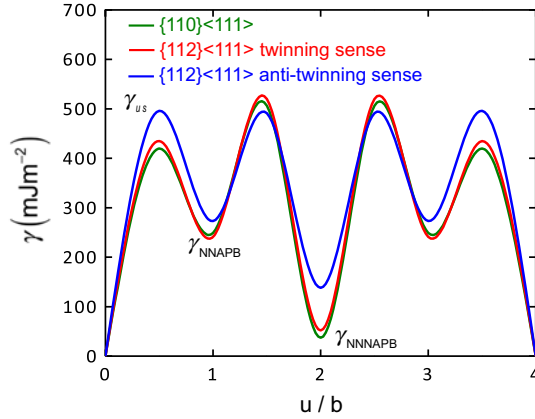

Figure 5. (colour online) GSFE for $D0_3$ Fe_3Al on $\{1\,1\,0\}\langle 1\,1\,1\rangle$ and $\{1\,1\,2\}\langle 1\,1\,1\rangle$ slip systems.

energy barriers between these two directions as the $\{1\,1\,2\}\langle 1\,1\,1\rangle$ slip asymmetry. For more details on twinning–antitwinning asymmetries in bcc metals, the reader is advised to see the Refs. [27–31]. We also note that the GSFE landscapes for $\{1\,1\,2\}\langle 1\,1\,1\rangle$ system in twinning sense and $\{1\,1\,0\}\langle 1\,1\,1\rangle$ system are similar. This is in agreement with other bcc metals as well, for example, bcc Fe [32,33].

Figure 6(a) and (b) show schematics of the stresses acting on the independently moving $a/4\langle 1\,1\,1\rangle$ superpartial during loading and unloading, respectively, and Figure 6(c) shows the corresponding stress regions of interest on the experimental stress–strain curve. Four independent stresses, τ_p, τ_b, τ_r, τ_o are shown. During loading (Figure 6(a)), the applied stress τ_p should overcome the frictional stress of the dislocation, τ_o and the back stress generated by the APB, τ_b. Upon unloading, the back stress (τ_b) generated by the $a/4\langle 1\,1\,1\rangle$ dislocation is balanced by the recovery start stress (τ_r) and the frictional stress (τ_o). In summary, the equations governing pseudoelasticity in Fe$_3$Al can be written as follows [4]:

$$\tau_p = \tau_b + \tau_o \tag{1}$$

$$\tau_r = \tau_b - \tau_o \tag{2}$$

In the present analysis, we solve for the Peierls stress τ_p and lattice frictional stress τ_o from Equation (1) and use it in Equation (2) to calculate the recovery start stress (τ_r). We present the results for $\{1\,1\,0\}\langle 1\,1\,1\rangle$ and $\{1\,1\,2\}\langle 1\,1\,1\rangle$ slips (both twinning and antitwinning senses), and the details of the analysis will follow later.
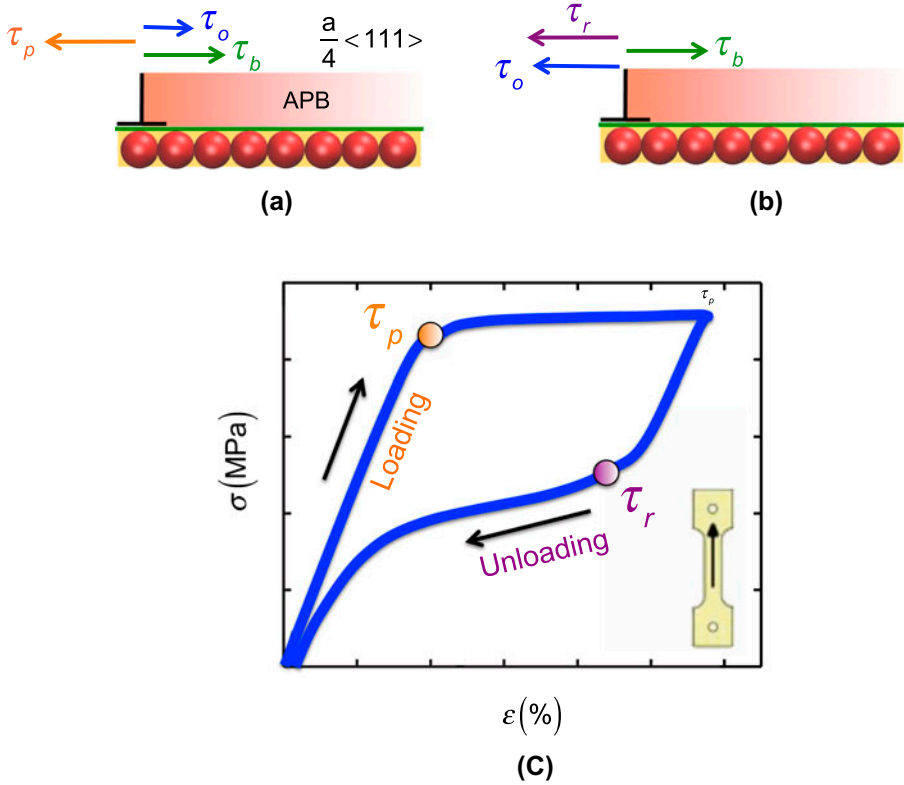

Figure 6. (colour online) Schematic representation of stresses acting on the uncoupled superpartial dislocation during (a) loading and (b) unloading. (c) A typical stress strain curve showing τ_p and τ_r.

3. Experimental procedures and observations

Fe$_3$Al single crystals were grown using the Bridgman technique in an inert atmosphere. Tensile dog-bone shaped specimens (1.5 mm × 3 mm net section and 10-mm gauge length) and compression specimens (4 mm × 4 mm × 10 mm) were cut using EDM. The crystal was oriented with the [1 5 11] crystallographic orientation parallel to the load direction where the primary slip system $[\bar{1}\,1\,1](1\,0\,1)$ has the maximum Schmid factor (SF) of 0.5. The specimens were then solution treated at 800 °C for 1 h and successively quenched in iced water. In order to obtain the D0$_3$ crystal structure, the specimens were annealed at 400 °C for 10 h and cooled in the furnace at room temperature. Following annealing, a virgin specimen was prepared for X-ray diffraction. The diffraction pattern and the pole figures were then obtained using a Philips Xpert 2 diffractometer. The lattice parameter was measured as $a = 5.785$ Å resulting in a close agreement with the one calculated with DFT. The crystal directions established with X-ray diffraction were [1 5 11] parallel to the load direction, $[1\,\overline{24}\,11]$ parallel to the normal of the specimen plane and $[\overline{11}\,0\,1]$ parallel to the specimen plane and perpendicular to the load direction.

Tensile and compression experiments were conducted at room temperature by means of a servo hydraulic load frame. The experiments were conducted in displacement control at a strain rate of approximately 5×10^{-5} s^{-1}. The average axial strains from DIC strain fields were used to construct the stress–strain curves, while the local strain values were used in order to precisely pinpoint the slip onset and recovery. An additional tensile experiment was conducted with a SEMtester load frame under an optical microscope for *in situ* high resolution strain measurements.

The specimens were initially polished using SiC paper (from P800 up to P1500). The speckle pattern was applied to the specimen's surface using black paint and an Iwata Micron B airbrush which enabled to produce a fine pattern on the surface adapted for both high and low DIC strain measurements. The images for *in situ* strain measurements under the servo hydraulic load frame were captured using an IMI model IMB-202 FT CCD camera (1600 × 1200 pixel) with a Navitar optical lens, providing an average resolution of 2 μm/px. The real-time strain measurements were obtained on a 3 mm × 2.25 mm region for the tensile specimens and for a 4 mm × 3 mm for the compression specimens. The images acquired during loading with the SEMtester load frame were captured under an Olympus BX51M microscope (Olympus lens) providing an average resolution of 0.44 μm/px. For this experimental set-up, the strain measurements were obtained for a region of 700 μm × 525 μm. For both set-ups, the first image is captured at zero load on the undeformed specimen's surface (herein referred as the reference image) while during loading, the images of the same region are captured every 2 s. In the strain plots appearing in Figures 7–9, we refer to the uniaxial tensile/compression ε strain parallel to the load direction as ε.

Figure 7 shows the stress–strain curves obtained in tension. The black line refers to the averaged axial strains measured all over the DIC region during the experiment carried out under the hydraulic load frame (image resolution with this set-up is 1.88 μm/px over 3 mm × 2.25 mm area). This curve represents the *bulk* mechanical behaviour of the single crystal. On the other side, the blue line refers to the experiment conducted with the SEMtester under the microscope (image resolution 0.44 μm/px). The axial strains are calculated averaging the DIC strain fields over a region of 700 μm × 525 μm
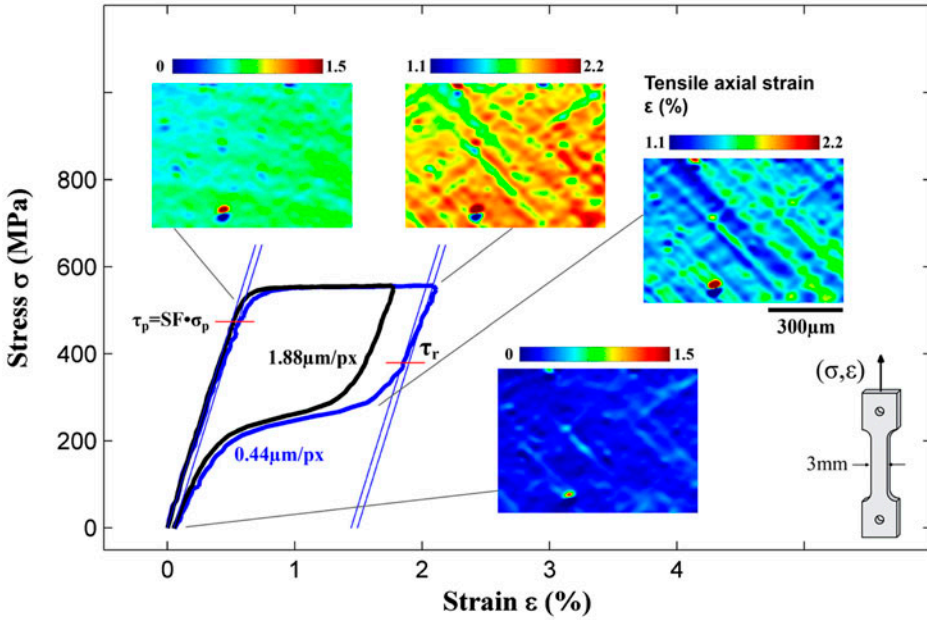
Figure 7. (colour online) Calculation of the critical applied stress τ_p and the recovery start stress τ_r from the stress–strain curves for the [1 5 11] crystal orientation in tension. The strain data marked with the black line were obtained averaging the strain fields over a region of 3 mm × 2.25 mm, while the strains marked with the blue line were calculated averaging the strain fields over a region of 700 μm × 525 μm. The applied stress τ_p and the recovery start stress τ_r are determined using the blue curve (for more details, see the text).

and are referred to as *local* strain measurements. Since the higher image resolution is obtained for this set-up, the observation of slip is obtained at the microscale allowing a precise estimation of the stress required to activate slip. The critical axial stresses (σ_p and σ_r) are obtained using the intersection between the blue curve and the line representing the elastic slope at 0.05% strain offset. The lines representing the elastic slopes are indicated in Figure 7. In both loading and unloading parts of the stress–strain curves, we report the line fitting the elastic region (the elastic modulus is calculated as 88 GPa) and a parallel line representing the elastic slope at 0.05% strain offset.

The critical applied stress τ_p and the recovery start stress τ_r are then calculated using the Schmid law, $\tau_p = SF \cdot \sigma_p$ and $\tau_r = SF \cdot \sigma_r$. The strain fields in Figure 8 show strain localizations along one slip trace, which confirms the activation of one dominant primary slip system.

In compression (Figure 9), the stress–strain behaviour of the [1 5 11] orientation is similar to the tensile case. The reported strain fields are measured by *in situ* DIC under the hydraulic load frame with a final image resolution of 2.37 μm/px (black line). In order to be consistent with the strain measurements provided for the tensile case under the SEMtester (see Figure 7), we calculate the local stress–strain curve (blue line) averaging the axial strains over a subregion of 800 μm × 600 μm (blue line). The first

Tensile axial strain ε (%) at maximum load
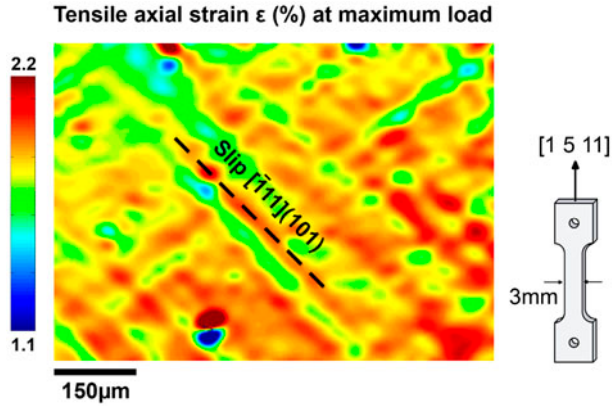
Figure 8. (colour online) Local strain measurements using high resolution DIC on a [1 5 11] oriented sample in tension. The broken line represents the $[\bar{1}\,1\,1](1\,0\,1)$ slip trace.

Fe₃Al - Single crystal [1 5 11] Compression

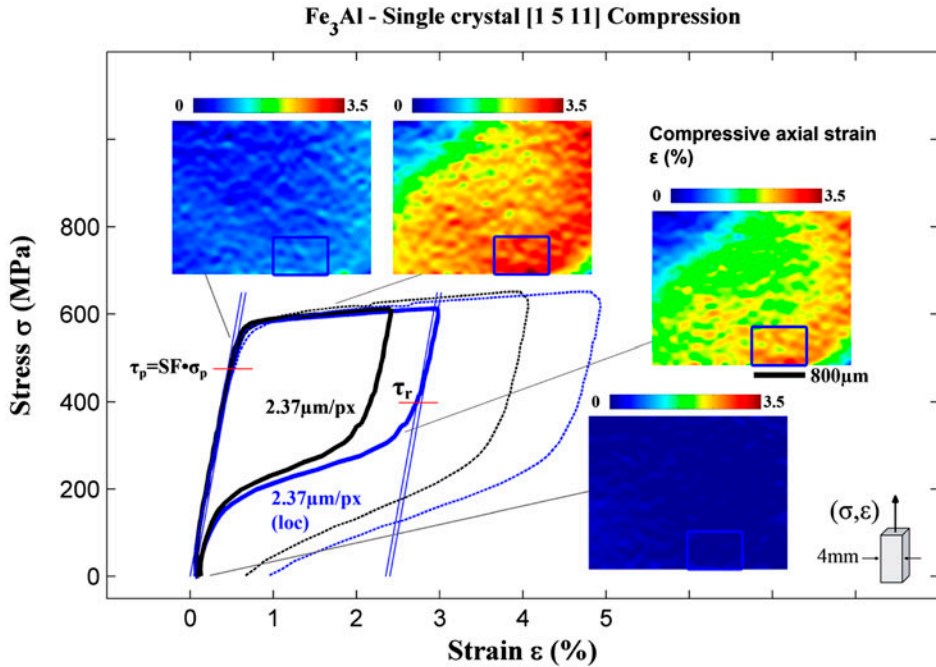Figure 9. (colour online) Stress–strain behaviour for the [1 5 11] crystal orientation in compression following two load/unload steps. The black lines refer to the averaged axial strain calculated over all the DIC area, while the blue lines refer to the local axial strains calculated for the subregion showing the largest strain localization (blue box marked in the bottom of each strain plot). The stress–strain behaviour during the first load step (continuum lines) is perfectly pseudoelastic, while during the second load step carried out at higher deformations (dashed lines), some residual strains remain upon unloading.

load step (black and blue continuum lines) shows a complete plastic recovery of 1.83% for the averaged strain over the entire region, while locally we measured a complete plastic recovery of 2.4%. During the second load step (black and blue dashed lines), the averaged plastic recovery was measured as 2.81%, while locally as 3.39%. Based on the localized stress–strain curves for the tensile and compressive experiments, we determined the averaged applied stress $\tau_p = 221$ MPa and the recovery start stress $\tau_r = 175$ MPa. Using Equations (1) and (2), we then calculate the back stress $\tau_b = 198$ MPa and the frictional stress $\tau_o = 23$ MPa.

4. Modelling of pseudoelasticity

We calculate the Peierls stress for slip nucleation [34,35] based on the modified PN formalism. The Peierls stress is calculated as the maximum slope of the misfit energy curve which describes the potential energy of the superpartials as a function of the positions [36,37]. The misfit energy can be derived from the GSFE as follows [36]:

$$E_{\text{misfit}} = \int_{-\infty}^{+\infty} \gamma_{\text{GSFE}}(f(x))\mathrm{d}x \tag{3}$$

where $f(x)$ is the disregistry function in terms of the dislocation position x, and represents the inelastic displacements across the glide plane of the dislocation. The solution to the disregistry function $f(x)$ involving multiple dislocations has been discussed in the literature [38]. Therefore, $f(x)$ for four superpartial dislocations can be written as follows:

$$f(x) = \frac{b}{\pi}\left(\tan^{-1}\left(\frac{x}{\xi}\right) + \tan^{-1}\left(\frac{x - d_1}{\xi}\right) + \tan^{-1}\left(\frac{x - (d_1 + d_2)}{\xi}\right)\right.$$
$$\left. + \tan^{-1}\left(\frac{x - (2d_1 + d_2)}{\xi}\right)\right) + 2b$$

The discrete form of Equation (3) can be written as:

$$E_{\text{misfit}} = \sum_{m=-\infty}^{m=+\infty} \gamma_{\text{GSFE}}(f(ma' - u))a' \tag{4}$$

where m is an integer, u is the position of the dislocation line, a' is the lattice periodicity defined as the shortest distance between two equivalent atomic rows in the direction of the dislocation displacement [34,39,40] and ξ is the half core width of the dislocation. The term $\gamma_{\text{GSFE}}(f(ma' - u))a'$ can be obtained for multiple dislocations [41]. It should be noted that the disregistry function incorporates the separation distance between the superpartials, d_1 and d_2. The following equations are used to find the separation distances [8].

$$\gamma_{\text{NNNAPB}} = K\left\{\frac{1}{d_1} + \frac{1}{d_1 + d_2} + \frac{1}{2d_1 + d_2}\right\}$$

$$\gamma_{\text{NNNAPB}} - \gamma_{\text{NNAPB}} = K\left\{\frac{1}{d_2} + \frac{1}{d_1 + d_2} - \frac{1}{d_1}\right\} \tag{5}$$

with γ and K representing the attraction and elastic repulsion force, respectively. The factor K is equal to $Gb^2/(2\pi)$, where G is the shear modulus of the slip system. The Peierls stress for dislocation slip is then calculated as follows:

$$\tau_p = \frac{1}{b}\max\left(\frac{\partial E_{\text{misfit}}}{\partial u}\right) \tag{6}$$

Figure 10 is the solution to Equation (4). The Peierls stress of 233 MPa is then calculated in the present analysis by taking the maximum slope of the misfit energy variation with respect to the dislocation position u.

4.1. *Lattice frictional stress (τ_o)*

We consider the total energy of the $a/4\langle 1\,1\,1\rangle$ superpartials. The total energy is expressed as the sum of (i) the line energies of the dislocations (E_{line}) (ii) the GSFE energy (E_{misfit}) and (iii) the elastic strain energy due to dislocations interaction, $E_{\text{interaction}}$. The total energy associated with the $a/4\langle 1\,1\,1\rangle$ superpartial dislocations can thus be expressed as follows:

$$E_{\text{total}} = E_{\text{line}} + E_{\text{misfit}} + E_{\text{interaction}} \tag{7}$$

Writing each of the energy terms in Equation (7), we have the following expression:

$$
\begin{aligned}
E_{\text{total}} = {} & \frac{nHC_{44}b^2}{4\pi}\ln\left(\frac{L}{r_o}\right) + \sum_{m=-\infty}^{m=+\infty}\gamma[f(ma'-u)]a' \\
& - \frac{HC_{44}b^2}{4\pi}\ln\left(\frac{L}{u-d_1} + \frac{L}{u-(d_1+d_2)+} + \frac{L}{u-(2d_1+d_2)}\right)
\end{aligned} \tag{8}
$$

In the above energy equation (8), H is the parameter that involves the orientation of the dislocation [42,43]. The parameter H can be written as follows:

$$H \approx 1 - 4\left(1 - A^{-1/2}\right)\left(\alpha^2\beta^2 + \gamma^2\alpha^2 + \beta^2\gamma^2\right)$$
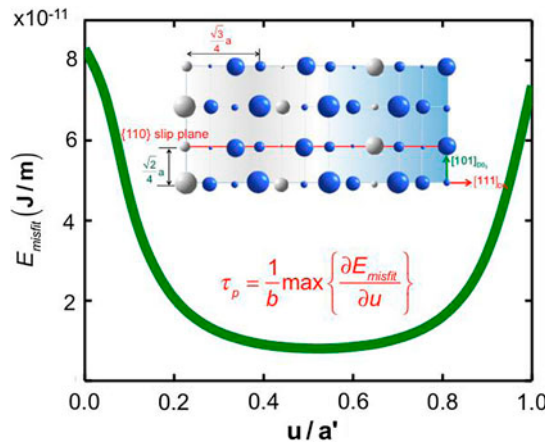

Figure 10. (colour online) Misfit energy variation with respect to dislocation positions for Fe$_3$Al.

where A is the Zener's anisotropy ratio of the crystal equal to $2C_{44}/(C_{11} - C_{12})$ and α, β, γ are the orientation of the dislocation line with respect to the cubic axes. The term n is the number of superpartials (equal to 4 in the present analysis) and b is the Burgers vector, u is the position of the dislocation line and L is the outer dimension of the crystal usually taken to be 500–1000 times the dislocation core width radius r_o. The lattice frictional stress, τ_o, can be determined by taking the derivative of the total energy with respect to u, i.e.

$$\tau_o = \frac{1}{b}\max\left(\frac{\partial E_{\text{total}}}{\partial u}\right) \tag{9}$$

We calculate τ_p as 233 MPa, τ_b as 199 MPa and τ_o as 34 MPa for $\{1\,1\,0\}\langle1\,1\,1\rangle$ slip. Utilizing Equations (1) and (2), τ_r is then calculated to be 165 MPa in the present analysis.

5. Discussion of the results

We established the GSFE curve for D0$_3$ Fe$_3$Al using first principles energy calculations, and incorporated it into the mesoscale elastic formulation to obtain the critical slip initiation stress during loading (τ_p), and the recovery start stress (τ_r) during unloading. We then experimentally determined the slip initiation and recovery start stresses using real-time high resolution strain measurements on compressive and tensile single crystal specimens precisely oriented for single slip. We note that for the case of $\{1\,1\,2\}\langle1\,1\,1\rangle$ slip, the frictional stress (τ_o) of superpartials during loading is different from unloading. This is because, if during loading, the superpartials move in the twinning sense, they move in the antitwinning sense during unloading and vice versa. We show that the frictional stress (τ_o) for the case of $\{1\,1\,2\}\langle1\,1\,1\rangle$ slip where superpartials move in the anitwinning sense is 93 MPa. We also observe that the τ_o is higher for the case of antitwinning sense than that of the twinning sense by 62 MPa. In such a case where loading/unloading asymmetry is observed, it should be noted that τ_o in Equations (1) and (2) will be different for forward and reverse loadings, and that τ_p and τ_r should be calculated using their respective values as follows:

$$\tau_p = \tau_b + (\tau_o)_f \tag{10}$$

$$\tau_r = \tau_b - (\tau_o)_r \tag{11}$$

where $(\tau_o)_f$ and $(\tau_o)_r$ are respectively the frictional stresses during forward loading and reverse unloading.

The results for three cases are presented in Table 4: (i) in case of $\{1\,1\,0\}\langle1\,1\,1\rangle$ slip where loading/unloading symmetry is not observed, $(\tau_o)_f$ for forward loading is the same as $(\tau_o)_r$ for reverse loading, (ii) in case of $\{1\,1\,2\}\langle1\,1\,1\rangle$ slip, when forward loading is in twinning sense and reverse unloading in antitwinning sense, $(\tau_o)_f$ for forward loading is the Peierls stress to move the superpartials in the twinning sense, and hence is lower than $(\tau_o)_r$ and, (iii) when forward loading is in antitwinning sense and reverse unloading in twinning sense for $\{1\,1\,2\}\langle1\,1\,1\rangle$ slip, the magnitude of $(\tau_o)_r$ is lower than $(\tau_o)_f$. It is worth noting that the loading orientation that tends to activate $\{1\,1\,2\}\langle1\,1\,1\rangle$ slip in antitwinning sense has to overcome a large stress (317 MPa) compared to the

stresses required to nucleate $\{1\,1\,0\}\langle 1\,1\,1\rangle$ and $\{1\,1\,2\}\langle 1\,1\,1\rangle$ slips in twinning sense. Therefore, the activation of $\{1\,1\,2\}\langle 1\,1\,1\rangle$ in antitwinning sense is unfavourable for a given loading orientation. Large recoverability is observed when one of the slip systems is activated. In case where both $\{1\,1\,0\}\langle 1\,1\,1\rangle$ and $\{1\,1\,2\}\langle 1\,1\,1\rangle$ slip systems are active, the latter are frequently observed to cross slip onto the $\{1\,1\,0\}$ plane forming jogged dislocations giving rise to numerous dipoles[4]. These dipoles hinder the reversible motion of the dislocations, and hence low recoverability is obtained. However, in the present case, the single crystal is oriented such that $\{1\,1\,0\}\langle 1\,1\,1\rangle$ slip systems are only activated, and hence large recovery is observed.

Table 4 also shows the experimental and theoretical values of the stresses obtained for Fe_3Al for $\{1\,1\,0\}\langle 1\,1\,1\rangle$ slip, and we note that the theoretically obtained values are within 10% of the experimental ones. It is worth noting from Table 4 that the set of stress values obtained from the theoretical calculations meets the condition for APB pseudoelasticity, which requires both τ_p and τ_r to have the same sense, tensile or compressive, during loading and unloading. A large magnitude of back stress (τ_b) of 199 MPa for $\{1\,1\,0\}\langle 1\,1\,1\rangle$ slip can easily pull the superpartials back during unloading overcoming the much smaller frictional stress (34 MPa) yielding a high recovery value.

Several factors such as degree of order, Al concentration, deformation temperature and loading orientation affect the reversibility value (r) of Fe_3Al [4,12]. Since pseudoelasticity in Fe_3Al can occur by pseudotwinning as well, the choice of orientation and deformation temperature is important. As pointed out in the literature [4], the core structure of $a/4\langle 1\,1\,1\rangle$ dislocations is considered similar to that of the $a/2\langle 1\,1\,1\rangle$ screw dislocation in a bcc crystal. Hence, similar to bcc metals, the deformation behaviour of Fe_3Al is greatly affected by the crystal orientation and temperature. We observed experimentally that Fe-23at.%Al shows up to 3.39% pseudoelastic recovery at room temperature. The reversibility value tends to decrease with the increase in Al concentration or a deviation in deformation temperature outside of 173–473 K regime. The reason behind this is that at extremely low temperatures, τ_o rapidly increases with decreasing temperature, while τ_b remains constant; and hence, the backward motion of dislocations become difficult at lower temperatures [3]. While in the higher temperature

Table 4. The critical slip nucleation stress and recovery start stress in $D0_3$ Fe_3Al for $\{1\,1\,0\}\langle 1\,1\,1\rangle$ and $\{1\,1\,2\}\langle 1\,1\,1\rangle$ slips obtained in the present analysis. The theoretically obtained values for $\{1\,1\,0\}\langle 1\,1\,1\rangle$ systems are compared to the experimentally measured values. The separation distances of the superpartials and the shear moduli are also given.

Slip systems	Critical shear stress (MPa)					Separation distances (nm)		Shear modulus (GPa)
	τ_p	τ_r	τ_b	$(\tau_o)_f$	$(\tau_o)_r$	d_1	d_2	
$\{1\,1\,0\}\langle 1\,1\,1\rangle$ (theory, present study)	233	165	199	34	–	20	30	21
$\{1\,1\,0\}\langle 1\,1\,1\rangle$ (experiments, present study)	221	175	198	23	–	8–10[8]	20–30	
$\{1\,1\,2\}\langle 1\,1\,1\rangle$ (forward load twinning sense)	226	102	195	31	93	14	22	22
$\{1\,1\,2\}\langle 1\,1\,1\rangle$ (forward load antitwinning sense)	317	193	224	93	31	12	22	

regime, the energy term γ_{NNAPB} diminishes exponentially such that the back stress is not large enough for dragging back the superpartials [3]. Our present analysis is relevant to the experimentally observed pseudoelasticity in Fe$_3$Al where slips are restricted to $\{1\,1\,0\}\langle1\,1\,1\rangle$ primary systems and deformed at room temperature.

Experimentally, we used tension and compression Fe$_3$Al single crystals oriented for single slip in order to capture τ_p and τ_r. DIC strain measurements were adopted in order to pinpoint these stresses. For example, if 0.2% strain offset of the macroscopic stress–strain curve was used to measure the stress, the slip nucleation stress for forward loading would be 266 MPa compared to the stress of 221 MPa obtained using DIC. This is a considerable difference. In general, strains measured with the extensometer overestimate the stress required to initiate slip since the early activation of slip on the microscale cannot be detected. On the other side, advanced DIC techniques used in conjunction with high resolution images under an optical microscope enable to measure the *local* stress–strain behaviour (Figures 7–9). In this work, a special load cell was used in order to load the specimen in tension under the optical microscope and capture the images at the resolution of 0.44 μm/px. The present experimental set-up is particularly important for studies on pseudoelasticity where the strains are recovered upon unloading and precise *real-time* strain measurements are required.

It is well known that pseudoelasticity is not observed in the L1$_2$ phase of Fe$_3$Al. This is the result of the high $\{1\,1\,0\}\langle1\,1\,1\rangle$ shear modulus (80 GPa compared to 21 GPa for D0$_3$ structure), and hence the high lattice frictional stress to initiate slip, as evident from Equations (8) and (9). The shear modulus of the slip system can be obtained from the maximum slope of the GSFE curve in Figure 5 [44]. For example, the shear modulus of $\{1\,1\,0\}\langle1\,1\,1\rangle$ system is approximately $G_{\{1\,1\,2\}\langle1\,1\,1\rangle} = 2\pi\frac{\partial\gamma}{\partial u}\big|_{\max} \sim 21$ GPa and that of $\{1\,1\,2\}\langle1\,1\,1\rangle$ slip system is 22 GPa from Figure 5. This is in accordance with the experimental value of 20 GPa for $\{1\,1\,2\}\langle1\,1\,1\rangle$ system using an alternative equation for shear modulus suggested by Roundy et al. [45]. Another reason for reduced or no pseudoelasticity in L1$_2$ phase is the lower back stress compared to the lattice frictional stress, and hence the dislocations cannot shuttle back and forth during loading and unloading. Other important factor that hinders pseudoelasticity is the activation and interaction of conjugate slips with the primary $\{1\,1\,0\}\langle1\,1\,1\rangle$ slips.

6. Conclusion

In summary, single crystals of Fe$_3$Al were selected in the D0$_3$ phase, and slip initiation stress was measured both in the tension and compression experiments in conjunction with high resolution DIC images. We utilized DFT calculations to obtain the energy barriers associated with the $\{1\,1\,0\}\langle1\,1\,1\rangle$ and $\{1\,1\,2\}\langle1\,1\,1\rangle$ slips both in twinning and antitwinning sense. Two important energy parameters, γ_{NNAPB} and γ_{NNNAPB} were established from DFT calculations, which were then combined with the mesoscale anisotropic elastic calculations to obtain the slip initiation and recovery start stress. The values we obtained from our theoretical calculations are within 10% of the experimentally observed values, reflecting a close agreement.

Disclosure statement

No potential conflict of interest was reported by the authors.

Funding

References

[1] K. Otsuka and C.M. Wayman (eds.), *Shape Memory Materials*, Cambridge University Press, Cambridge, 1998.

[2] H.Y. Yasuda, K. Kouzai, Y. Kawamura and Y. Umakoshi, ISIJ Int. 50 (2010) p.147.

[3] H.Y. Yasuda and Y. Umakoshi, Intermetallics 18 (2010) p.1273.

[4] H.Y. Yasuda and Y. Umakoshi, *Pseudoelasticity of D03-type Fe3Al and Fe3Ga-based alloys*, in *Mater. Res. Soc. Symp. Proc*, Boston, MA, 2011, p.5.

[5] L.P. Kubin, A. Fourdeux, J.Y. Guedou and J. Rieu, Philos. Mag. A 46 (1982) p.357.

[6] A. Brinck, C. Engelke, H. Neuhäuser, G. Molénat, H. Rösner, E. Langmaack and E. Nembach, Mater. Sci. Eng., A 258 (1998) p.32.

[7] H.Y. Yasuda, K. Nakano, T. Nakajima, M. Ueda and Y. Umakoshi, Acta Mater. 51 (2003) p.5101.

[8] R.C. Crawford, I.L.F. Ray and D.J.H. Cockayne, Philos. Mag. 27 (1973) p.1.

[9] J.Y. Guedou, M. Paliard and J. Rieu, Scr. Metall. 10 (1976) p.631.

[10] E. Langmaack and E. Nembach, Philos. Mag. A 79 (1999) p.2359.

[11] Y. Umakoshi, T. Nakajima and H.Y. Yasuda, *Effects of dislocation and microstructure on pseudoelasticity in D03-type Fe3Al single crystals*, in *MRS Proceedings*, Cambridge University Press, Cambridge, 2006, p.0980.

[12] H.Y. Yasuda, K. Yamaoka, Y. Oda and Y. Umakoshi, Scr. Mater. 59 (2008) p.738.

[13] M.J. Marcinkowski and N. Brown, Acta Metall. 9 (1961) p.764.

[14] H.Y. Yasuda, T. Nakajima, K. Nakano, K. Yamaoka, M. Ueda and Y. Umakoshi, Acta Mater. 53 (2005) p.5343.

[15] H.Y. Yasuda, K. Fukushima, M. Aoki and Y. Umakoshi, ISIJ Int. 48 (2008) p.1014.

[16] J.D. Carroll, W. Abuzaid, J. Lambros and H. Sehitoglu, Int. J. Fatigue 57 (2013) p.140.

[17] A. Ojha, H. Sehitoglu, L. Patriarca and H.J. Maier, Philos. Mag. 94 (2014) p.1816.

[18] G.J. Pataky, M.D. Sangid, H. Sehitoglu, R.F. Hamilton, H.J. Maier and P. Sofronis, Eng. Fract. Mech. 94 (2012) p.13.

[19] L. Patriarca, W. Abuzaid, H. Sehitoglu, H.J. Maier and Y. Chumlyakov, Mater. Charact. 75 (2013) p.165.

[20] G. Kresse and J. Furthmüller, Phys. Rev. B 54 (1996) p.11169.

[21] G. Kresse and J. Hafner, Phys. Rev. B 48 (1993) p.13115.

[22] W.B. Pearson, *Lattice Spacings and Structures of Metals and Alloys*, Vol. 884, Pergamon, Oxford, 1958.

[23] D. Connétable and P. Maugis, Intermetallics 16 (2008) p.345.

[24] H.J. Leamy, E.D. Gibson and F.X. Kayser, Acta Metall. 15 (1967) p.1827.

[25] V. Vítek, Philos. Mag. 18 (1968) p.773.

[26] A. Ojha, H. Sehitoglu, L. Patriarca and H.J. Maier, Modell. Simul. Mater. Sci. Eng. 22 (2014) p.075010.

[27] M.S. Duesbery and V. Vitek, Acta Mater. 46 (1998) p.1481.

[28] V. Vitek, *Computer simulation of the screw dislocation motion in bcc metals under the effect of the external shear and uniaxial stresses*, *Proceedings of the Royal Society of London A: Mathematical, Physical and Engineering Sciences*, The Royal Society, London, 1976, p.109.

[29] K. Ito and V. Vitek, Philos. Mag. A 81 (2001) p.1387.

[30] J.W. Christian, Metall. Trans. A 14 (1983) p.1237.

[31] M. Yamaguchi and V. Vitek, J. Phys. F: Met. Phys. 5 (1975) p.11.

[32] S. Li, X. Ding, J. Deng, T. Lookman, J. Li, X. Ren, J. Sun and A. Saxena, Phys. Rev. B 82 (2010) p.205435.

[33] L. Ventelon and F. Willaime, Philos. Mag. 90 (2010) p.1063.

[34] B. Joós and M.S. Duesbery, Phys. Rev. Lett. 78 (1997) p.266.

[35] B. Joós, Q. Ren and M.S. Duesbery, Phys. Rev. B 50 (1994) p.5890.

[36] Y.-M. Juan and E. Kaxiras, Philos. Mag. A 74 (1996) p.1367.

[37] E.B. Tadmor and R.E. Miller, *Modeling Materials*, Cambridge, Cambridge University Press, 2011.

[38] J. Wang and H. Sehitoglu, Modell. Simul. Mater. Sci. Eng. 22 (2014) p.055008.

[39] L. Lejček, Czech. J. Phys. 26 (1976) p.294.

[40] G. Schoeck, Phys. Rev. Lett. 82 (1999) p.2310.

[41] J. Wang and H. Sehitoglu, Comput. Mater. Sci. 87 (2014) p.34.

[42] A.K. Head, Phys. Status Solidi (b) 6 (1964) p.461.

[43] A.K. Head, Phys. Status Solidi (b) 5 (1964) p.51.

[44] R.W. Hertzberg, *Deformation and Fracture Mechanics of Engineering Materials*, John Wiley and Sons, New York, NY, 1996.

[45] D. Roundy, C.R. Krenn, M.L. Cohen and J.W. Morris Jr., Phys. Rev. Lett. 82 (1999) p.2713.